Gravitational waves produced by domain walls during inflation

Haipeng An[1,2,3,4,*] and Chen Yang[1,†]

[1]*Department of Physics, Tsinghua University, Beijing 100084, China*
[2]*Center for High Energy Physics, Tsinghua University, Beijing 100084, China*
[3]*Center for High Energy Physics, Peking University, Beijing 100871, China*
[4]*Frontier Science Center for Quantum Information, Beijing 100084, China*

(Received 14 May 2023; accepted 1 May 2024; published 3 June 2024)

We study the properties of the stochastic gravitational-wave background (SGWB) produced by domain walls (DWs) during inflation without forming a network. We numerically simulate the DW production caused by a second-order phase transition and calculate the SGWB spectrum using a $1000 \times 1000 \times 1000$ lattice. We show that the SGWB can be observed directly by future terrestrial and space gravitational-wave detectors and through the B-mode spectrum in the cosmic microwave background. With numerical simulations, we derive an empirical formula for the strength and qualitative features of the SGWB spectrum. The details of the SGWB spectrum also contain information about the later evolution of the Universe.

DOI: 10.1103/PhysRevD.109.123508

I. INTRODUCTION

The direct discovery of gravitational waves (GWs) produced by black hole binary mergers opened up a new era of GW astrophysics [1]. GWs can also be produced in the early Universe via phase transitions, topological defects, scalar perturbations, and quantum fluctuation during inflation, forming the stochastic GW background (SGWB). See Ref. [2] for an excellent review and references therein. Once produced, GWs propagate almost freely through the Universe, bringing us information about their origin and the evolution of the Universe. Terrestrial and space-based detectors are proposed to search for SGWB [3–15]. SGWB with a frequency around 10^{-8} Hz can be detected via radio telescopes using the pulsar timing arrays (PTAs) [11,16,17]. The common noise process observed by the PTAs might indicate a signal of SGWB [18–21]. SGWB with longer wavelengths may also imprint on the cosmic microwave background (CMB) and be detected via the B-mode spectrum [22–24].

One important source of SGWB that has been extensively studied in the literature is the cosmic domain walls (DWs) [25–32] (for a review, see [33]). DW-induced GWs as a test for new physics beyond the standard model have attracted a lot of interests in the literature [34–42]. DWs are two-dimensional topological defects created via the spontaneous breaking of discrete symmetries. Stable domain walls will form a network in the radiation-domination (RD) era and overclose the Universe [25]. Thus, an explicit symmetry-broken term is usually introduced to ensure that the DWs annihilate before big bang nucleosynthesis [26–28]. Traditional studies of SGWB produced by DWs focus on production through the DW network. Both qualitative analysis [29] and numerical simulations [30] show that the GW energy density production rate by the DW network is constant during RD. Therefore, the GWs produced right before the annihilation of the DWs dominate the contribution to the SGWB energy density today since they are the least redshifted. However, if the DWs annihilate too early, the SGWB signal will be too weak to induce detectable signals in future GW detectors.

In this paper, we point out that if the DWs were produced during inflation, they would generate SGWB during inflation without forming a network, and the strength of the SGWB can reach the sensitivities of the planned GW detectors. In flat space-time or during the RD era, static sources cannot radiate GWs due to energy conservation. However, during inflation, the Hubble expansion rate is significant and thus energy is no longer conserved. Therefore, even *comovingly static* sources can produce GWs. If the DWs are produced about 60 e-folds before the end of inflation, the SGWB will induce a CMB B-mode spectrum that future CMB observatories can detect. If the phase transition occurs at about 40 e-folds before the end of inflation, the SGWB the DWs produced will be able to explain the common noise process observed by PTAs [18–21].

*anhp@mail.tsinghua.edu.cn
†yangc18@mails.tsinghua.edu.cn

This paper is organized as follows. In Sec. II we describe the property of second-order phase transitions and the formation of DWs during inflation. Then, we show the numerical results of the SGWB signal in Sec. III and the semianalytical derivation of the SGWB signal in Sec. IV. The calculation of the SGWB signal's redshift factor for different Universe evolutions is shown in Sec. V. Next, we discuss the detectability of our SGWB signal in Sec. VI. Finally, we summarize our results in Sec. VII. In the Appendix we present the numerical algorithm used in our simulation.

II. PRODUCTION OF DWs DURING INFLATION

This work studies the phase transition in a spectator sector during de Sitter inflation. We use comoving coordinates with the conformal time, and the background de Sitter metric can be written as

$$ds^2 = a^2(\tau)(d\tau^2 - dx^2 - dy^2 - dz^2), \tag{1}$$

where $a(\tau) = -1/H\tau$ is the scale factor. The Lagrangian of the spectator can be written as

$$\mathcal{L} = \frac{1}{2H^2\tau^2}[\sigma'^2 - \nabla\sigma\cdot\nabla\sigma] - \frac{1}{H^4\tau^4}V(\sigma), \tag{2}$$

where σ is the spectator field and serves as the order parameter for the second-order phase transition, and the primes indicate derivatives with respect to τ. We assume that the potential is of the Landau-Ginzburg type,

$$V = \frac{1}{2}m_{\rm eff}^2\sigma^2 + \frac{\lambda}{4}\sigma^4. \tag{3}$$

We consider two scenarios. In scenario (A), we assume that the Universe was in RD before inflation. At the beginning of inflation, the temperature of the thermal plasma quickly falls and thus a phase transition happens in the plasma. This scenario has been considered in the context of grand unification models [43]. In this case, we have $m_{\rm eff}^2 = yT^2 - m^2$, where T is the temperature in the spectator sector, m is the mass of σ at zero temperature, and y is a constant parameter. In this scenario, the phase transition happens at the critical temperature $T_c = y^{-1/2}m$. In scenario (B), we consider an inflaton-driven phase transition similar to the study of first-order phase transitions in Refs. [44,45]. We observe that in large-field inflation models, the excursion of the inflaton field can be as large as the Planck scale. Thus, if we assume that the spectator fields are directly coupled to the inflaton field, the evolution of the inflaton field may induce dramatic changes of the masses or couplings in the spectator sector and thus lead to phase transitions during inflation. The effective mass can be written as $m_{\rm eff}^2 = y\phi^2 - m^2$, where ϕ is the inflaton field.

Now we describe the qualitative features of evolution and the DW formation process. The production of the topological defects can be described by the Kibble-Zurek mechanism [46,47]. Around the critical time τ_c, we can use the potential

$$V_{\rm KZ} = -\frac{1}{2}m_{\rm KZ}^3 a_c(\tau - \tau_c)\sigma^2 + \frac{\lambda}{4}\sigma^4 \tag{4}$$

to describe the evolution of σ, where $a_c \equiv a_{\tau=\tau_c}$. For scenarios (A) and (B), the Kibble-Zurek scale $m_{\rm KZ}$ can be written as [48]

$$\begin{aligned} m_{{\rm KZ}(A)}^3 &= -ya_c^{-1}\left.\frac{dT^2}{d\tau}\right|_{\tau=\tau_c} = 2m^2H, \\ m_{{\rm KZ}(B)}^3 &= -ya_c^{-1}\frac{d\phi_0^2}{d\tau} = \frac{2^{3/2}\epsilon^{1/2}m^2HM_{\rm pl}}{\phi_0(\tau_c)}, \end{aligned} \tag{5}$$

where ϵ is the slow-roll parameter and ϕ_0 is the homogeneous part of ϕ. In the simplest slow-roll model, $\phi_0(\tau_c) \approx N_c(2\varepsilon)^{1/2}M_{\rm pl}$ [49], where N_c is the e-folds between the critical point and the end of inflation. Therefore, compared to (A), $m_{\rm KZ}$ in (B) is suppressed by a factor of $N_c^{1/3}$. In this work, for the phase transition to complete during inflation, we assume that m is large enough such that $m_{\rm KZ} \gg H$.

To study the dynamics of this second-order phase transition, we follow the strategy in Ref. [50] and generalize the discussions in [50] to de Sitter space.

Right after the phase transition, the nonlinear term $\lambda\sigma^4$ is negligible. The Hamiltonian that governs the evolution of σ is

$$\begin{aligned} \mathscr{H} &= \int d^3\mathbf{x}\frac{1}{2}\left[\frac{1}{a^2}\pi^2 + a^2(\nabla\sigma)^2 + a^4m_{\rm eff}^2\sigma^2\right] \\ &= \int \frac{d^3\mathbf{k}}{(2\pi)^2}\frac{1}{2}\left[\frac{1}{a^2}\tilde{\pi}^2 + (a^2k^2 + a^4m_{\rm eff}^2)\tilde{\sigma}^2\right], \end{aligned} \tag{6}$$

where

$$\pi \equiv a^2\sigma' \tag{7}$$

is the canonical momentum and the tilde denotes the Fourier transform. The Fourier modes of σ and π satisfy the Hamiltonian equations of motion

$$\frac{d}{d\tau}\begin{pmatrix}\tilde{\pi}\\ \tilde{\sigma}\end{pmatrix} = \begin{pmatrix}0 & -(a^2k^2 + a^4m_{\rm eff}^2)\\ a^{-2} & 0\end{pmatrix}\begin{pmatrix}\tilde{\pi}\\ \tilde{\sigma}\end{pmatrix}. \tag{8}$$

To quantize the theory, we impose the equal-time canonical commutation relation to σ,

$$[\sigma(\mathbf{x},\tau), \pi(\mathbf{y},\tau)] = i\delta^3(\mathbf{x}-\mathbf{y}). \tag{9}$$

We expand σ by ladder operators $a_{\mathbf{k}}, a^{\dagger}_{-\mathbf{k}}$. The solution can be expressed as

$$\tilde{\pi}(\mathbf{k},\tau) = a_{\mathbf{k}} a(\tau)^2 f'(k,\tau) + a^{\dagger}_{-\mathbf{k}} a(\tau)^2 f'^{*}(k,\tau), \quad (10)$$

$$\tilde{\sigma}(\mathbf{k},\tau) = a_{\mathbf{k}} f(k,\tau) + a^{\dagger}_{-\mathbf{k}} f^{*}(k,\tau), \quad (11)$$

where the mode function f depends only on k since the space is homogeneous and isotropic and satisfies the equation of motion

$$f'' - \frac{2f'}{\tau} + \left(k^2 + \frac{m_{\mathrm{eff}}^2}{H^2\tau^2}\right) f = 0. \quad (12)$$

We require the ladder operators to satisfy the commutation relation

$$[a_{\mathbf{k}}, a^{\dagger}_{\mathbf{q}}] = (2\pi)^3 \delta^3(\mathbf{k}-\mathbf{q}). \quad (13)$$

This leads to the normalization condition for the mode function,

$$a(\tau)^2 (f(k,\tau) f'^{*}(k,\tau) - f'(k,\tau) f^{*}(k,\tau)) = i. \quad (14)$$

The time scale of the phase transition is determined by m_{KZ}, which is much larger than H, and thus when setting the initial condition of f at τ_c we can neglect the Hubble expansion. Therefore, just as in [50], we choose

$$f(k,\tau_c) = \frac{1}{a(\tau_c)} \frac{1}{\sqrt{2k}} e^{-ik\tau_c},$$
$$f'(k,\tau_c) = \frac{-i}{a(\tau_c)} \sqrt{\frac{k}{2}} e^{-ik\tau_c} \quad (15)$$

as the initial condition for (12).

The modes become classical when the anticommutator of $\tilde{\sigma}_{\mathbf{k}}$ and $\tilde{\pi}_{\mathbf{k}}$ is significantly larger than their commutator,

$$|\langle [\hat{\tilde{\sigma}}_{\mathbf{k}}(\tau), \hat{\tilde{\pi}}_{\mathbf{k}}(\tau)]_{+} \rangle| \gg |\langle [\hat{\tilde{\sigma}}_{\mathbf{k}}(\tau), \hat{\tilde{\pi}}_{\mathbf{k}}(\tau)] \rangle|, \quad (16)$$

where the expectation value is over the temporary vacuum state at τ_c. This is equivalent to requiring

$$F(k,\tau) \gg 1, \quad (17)$$

where the function F is defined as

$$F(k,\tau) = a(\tau)^2 \mathrm{Re}[f'(k,\tau) f^{*}(k,\tau)]. \quad (18)$$

Plots of $f(k)$ and $F(k)$ are shown in Figs. 1 and 2 for different values of ka_c^{-1} and H separately. In these plots, to compare with the Minkowski space ($H = 0$) result in [50], we use the physical time t in Fig. 2, defined as $dt = ad\tau$. One can see that F grows exponentially after the phase transition for the modes with $ka_c^{-1} < \mathcal{O}(m_{\mathrm{KZ}})$ as long as H is significantly smaller than m_{KZ}.

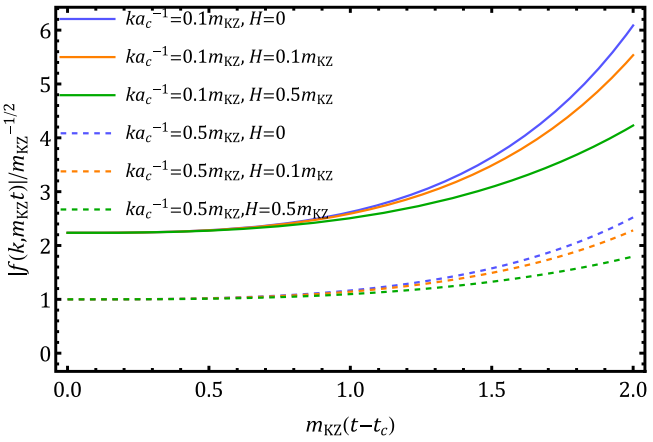

FIG. 1. Evolution of the mode function $f(k)$ as a function of the physical time t for different values of ka_c^{-1} and H.

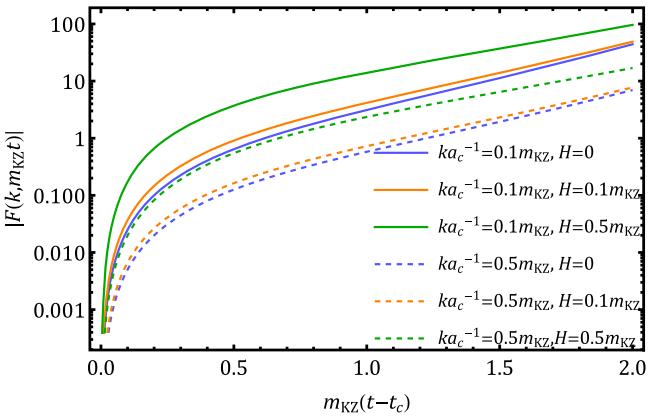

FIG. 2. $F(k)$ as a function of physical time t for different values of ka_c^{-1} and H.

Then, the canonical phase-space distribution of the long-wavelength modes can be described by the Gaussian ensemble given by the Wigner function [51–53]

$$W_{\mathbf{k}}(\tilde{\sigma}_{\mathbf{k}}, \tilde{\pi}_{\mathbf{k}}) = \frac{1}{\pi^2} \exp\left[-\frac{|\sigma_{\mathbf{k}}|^2}{|f(\mathbf{k},\tau)|^2} - 4|f(\mathbf{k},\tau)|^2 \left| \pi_{\mathbf{k}} - \frac{F(\mathbf{k},\tau)}{|f(\mathbf{k},\tau)|^2} \sigma_{\mathbf{k}} \right|^2 \right]. \quad (19)$$

After τ_c, due to the tachyonic growth, the nonlinear term $\lambda\sigma^4$ becomes more and more important, and then when we consider the evolution of $\tilde{\sigma}(\mathbf{k})$ we must include the back-reaction from the long-wavelength modes. Thus, the linearized equation of motion for $\tilde{\sigma}(\mathbf{k})$ can be written as

$$\sigma''_{\mathbf{k}} + \frac{2a'}{a} \sigma'_{\mathbf{k}} + \omega_{\mathbf{k}}^2(\tau) \sigma_{\mathbf{k}} = 0, \quad (20)$$

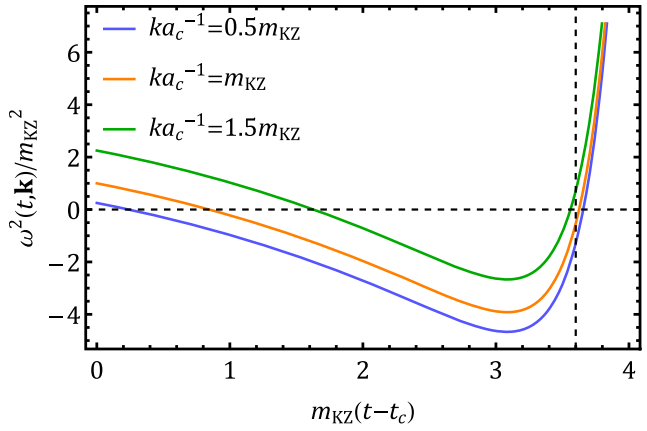

FIG. 3. Evolution of $\omega_{\mathbf{k}}^2$ as a function of the physical time t for different values of ka_c^{-1} and H.

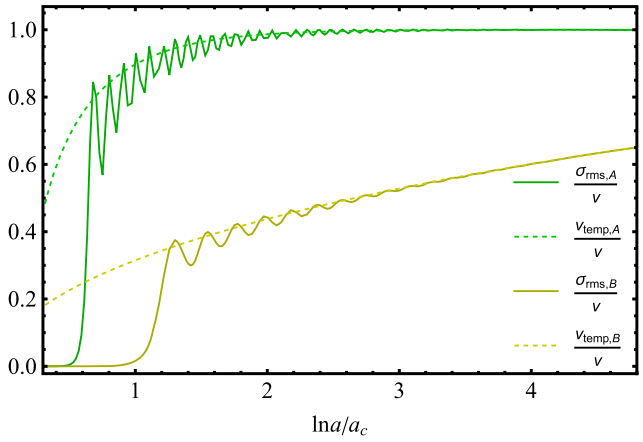

FIG. 4. Evolutions of the root-mean-square of σ for scenarios (A) (green) and (B) (yellow). The dashed curves show the corresponding temporary expectation of σ. For both cases, we use $H=10^{-4}M_{\rm pl}$, $m=5\times10^{-3}M_{\rm pl}$. For (A) we have $\lambda=0.0625$, $m_{\rm KZ}=(2m^2H)^{1/3}$, and for (B) we have $\lambda=0.004$ and $m_{\rm KZ}=0.126m$.

with

$$\omega_{\mathbf{k}}^2 = k^2 - a(\tau)^2(m_{\rm KZ}^3 a_c(\tau-\tau_c) - 3\lambda\langle\sigma^2(\tau,\mathbf{x})\rangle), \quad (21)$$

where the expectation value of $\langle\sigma^2(\tau,\mathbf{x})\rangle$ includes all of the contributions from the long-wavelength modes that have grown exponentially. Figure 3 shows the evolution of ω^2 for different values of k with $H=0.1m_{\rm KZ}$ and $\lambda=0.1$. Note that $\sigma(\mathbf{k})$ can grow tachyonically only when $\omega^2<0$. Thus, one can see that only modes with $k<\mathcal{O}(m_{\rm KZ})$ can grow tachyonically. We should note that the time span for $\omega^2<0$ is not sensitive to the value of λ, since after the phase transition $\langle\sigma^2(\mathbf{x})\rangle$ grows as $e^{[m_{\rm KZ}(t-t_c)]^3}$.

Around τ_c, σ is still located at 0; thus, $\langle\sigma^2(\tau)\rangle$ can be neglected. Therefore, $\omega_{\mathbf{k}}^2$ is negative for the infrared modes with small enough k^2, and thus $\sigma_{\mathbf{k}}$ grows exponentially. After a while, when the nonlinear term in the potential becomes important, the exponential growth stops. Our numerical simulation shows that only modes with $ka_c^{-1}<\mathcal{O}(m_{\rm KZ})$ can experience exponential growth. Due to the exponential growth, the particle numbers for long-wavelength modes are large. Thus, we can use the classical Gaussian random field to approximate the quantum modes to set the initial condition for the nonlinear evolution. Then, we use a $1000\times1000\times1000$ lattice to simulate the nonlinear evolution classically. The details of our numerical simulation algorithm are presented in the Appendix.

Following [50], we use $m_{\rm KZ}(t-t_c)=2$ as the matching point between tachyonic growth and the nonlinear classical evolution. Specifically, we numerically solve Eq. (12) with the initial condition (15). Then, at $m_{\rm KZ}(t-t_c)=2$ we randomly generate $\tilde{\sigma}(\mathbf{k})$ and $\tilde{\pi}(\mathbf{k})$ according to the distribution function (19). Then, from $\tilde{\sigma}$ and $\tilde{\pi}$, we calculate the initial configuration of $\sigma(\mathbf{x})$ and $\pi(\mathbf{x})$ for the classical lattice simulation of the nonlinear evolution.

Figure 4 shows the evolution of the temporary root-mean-square of σ for scenarios (A) and (B) together with the temporary vacuum expectation values $v_{\rm temp}\equiv\lambda^{-1/2}m_{\rm eff}$. The curves for $\sigma_{\rm rms}$ and $v_{\rm temp}$ are normalized to $v=\lambda^{-1/2}m$. One can see that in (A), since the temperature T redshifts as a^{-1}, $v_{\rm temp}$ approaches v after about one e-fold. However, in (B), since the evolution is driven by ϕ_0, $v_{\rm temp}$ will not reach v until the end of inflation. At the beginning of the phase transition, the growth of $\sigma_{\rm rms}$ lags behind $v_{\rm temp}$, which causes the oscillations of $\sigma_{\rm rms}$ around $v_{\rm temp}$. As a result, $\sigma_{\rm rms}$ oscillates around $v_{\rm temp}$ in the later oscillation. However, the oscillation is significantly damped after several e-folds due to the Hubble friction. Then, the σ-field configuration becomes *comovingly static*, which means that the shape of the configuration does not change comovingly, and the physical thickness of the walls is fixed. The configurations for σ at different times are shown in Figs. 5 and 6. In both cases, the field configuration becomes *static* after several e-folds. One can see that once the DWs are formed, their comoving density does not change and the average distance between the walls is about $2\pi m_{\rm KZ}^{-1}a_c^{-1}$, as predicted, since only modes with $ka_c^{-1}<\mathcal{O}(m_{\rm KZ})$ can grow exponentially.

III. GW PRODUCTION DURING QUASI–DE SITTER INFLATION

The Fourier modes of the tensor perturbation, $\tilde{h}_{ij}(\tau,\mathbf{k})$, satisfy the linearized Einstein equation

$$\tilde{h}_{ij}''(\tau,\mathbf{k}) + \frac{2a'}{a}\tilde{h}_{ij}'(\tau,\mathbf{k}) + k^2\tilde{h}_{ij}(\tau,\mathbf{k}) = 16\pi G_N\tilde{T}_{ij}^{TT}(\tau,\mathbf{k}), \quad (22)$$

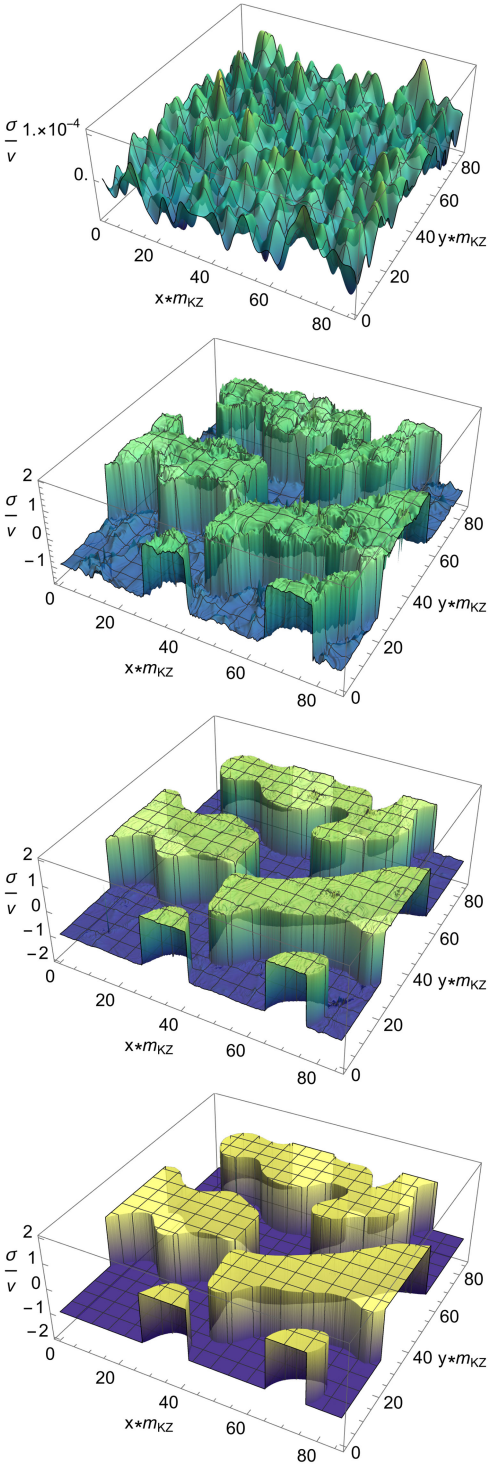

FIG. 5. Evolution of the σ field in scenario (A) for $\ln a/a_c = 1.3$, 2.3, 3.3, and 4.3, where the x and y axes show the comoving coordinates in units of $a_c^{-1}m_{\mathrm{KZ}}^{-1}$ and the z axis shows σ/v. The parameters in the potential are the same as in Fig. 4.

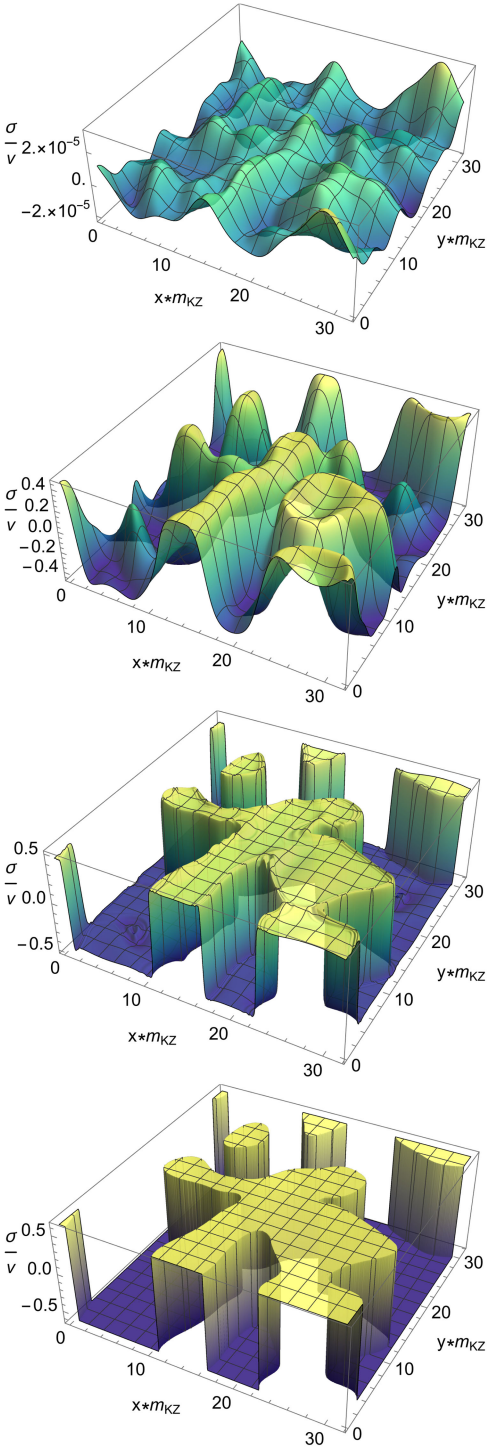

FIG. 6. Evolution of the σ field in scenario (B), where the labels of the axes are the same as in Fig. 5. The parameters in the potential are the same as in Fig. 4.

where $\tilde{T}_{ij}^{TT}$ is the transverse-traceless part of the energy-momentum tensor and can be written as

$$\tilde{T}_{ij}^{TT}(\tau,\mathbf{k}) = \int \frac{d^3p}{(2\pi)^3}\Lambda_{ij,kl}p^k p^l \tilde{\sigma}(\tau,\mathbf{p})\tilde{\sigma}(\tau,\mathbf{k}-\mathbf{p}), \quad (23)$$

where $\Lambda_{ij,kl} = \mathcal{P}_{ik}\mathcal{P}_{jl} - \frac{1}{2}\mathcal{P}_{ij}\mathcal{P}_{kl}$ is the projection operator and $\mathcal{P}_{ij} = \delta_{ij} - \hat{k}_i\hat{k}_j$.

During inflation, when $\tilde{h}(\tau,\mathbf{k})$ leaves the horizon ($k|\tau| < 1$), they will be frozen to a fixed value $\tilde{h}^f(\mathbf{k})$. After inflation, when the mode reenters the horizon, $\tilde{h}^f$ will serve as the amplitude for later evolution. Then, the general form of $\tilde{h}(\tau,\mathbf{k})$ is

$$\tilde{h}_{ij}(\tau,\mathbf{k}) = \tilde{h}_{ij}^f(\mathbf{k})\tilde{\mathcal{E}}_0^i(k)a^{-1}\sin(k\tau+\phi), \quad (24)$$

where $\tilde{\mathcal{E}}_0^i$ and ϕ are determined by the evolution of the Universe before the mode reenters the horizon. The detailed forms of $\tilde{\mathcal{E}}_0^i(k)$ and ϕ can be found in [45]. Then, we calculate the GW energy density spectrum,

$$\frac{d\rho_{\rm GW}}{d\ln k} = \frac{k^5|\tilde{\mathcal{E}}_0^i(k)|^2}{64\pi^3 G_N a^4}\frac{\langle|\tilde{h}_{ij}^f(\mathbf{k})|^2\rangle}{V}, \quad (25)$$

where G_N is the Newton gravity constant and V is the total comoving volume, which will be canceled by the same volume factor in $\langle|\tilde{h}_{ij}^f(\mathbf{k})|^2\rangle$.

Using Green's function method, we can calculate $\tilde{h}^f$ [44,45],

$$\tilde{h}_{ij}^f(\mathbf{k}) = \frac{16\pi G_N}{k}\int_{-\infty}^{0} d\tau' \mathcal{K}(k\tau')\tilde{T}_{ij}^{TT}(\tau',\mathbf{k}), \quad (26)$$

where $\mathcal{K}$ is the integral kernel,

$$\mathcal{K}(\eta) = \frac{1}{\eta}\left(\cos\eta - \frac{\sin\eta}{\eta}\right). \quad (27)$$

Equation (26) indicates that during inflation GWs can even be produced by a stationary source because the time translation symmetry is badly broken. The plot of $\mathcal{K}$ is shown in Fig. 7, from which we can see that the highest peak of $\mathcal{K}$ is around $k\tau' \approx -2$, and this is the moment $\tilde{T}_{ij}^{TT}(\tau',\mathbf{k})$ contributes the most to $\tilde{h}_{ij}^f(\mathbf{k})$.

After doing a small-$k\tau'$ expansion in the integral (26), we can see that the integral is finite at $\tau' = 0$ and thus the integral is mainly contributed in the region $k\tau' \sim -2$. Figure 8 shows the spectrum of $|\tilde{h}_{ij}^f|^2/V$ accumulated from τ_c to $\ln(a/a_c) = 1.3, 2.3, 3.3, 4.3$ for both scenarios (A) and (B). One can see that the GW productions for both scenarios stop at about four e-folds after the phase transition.

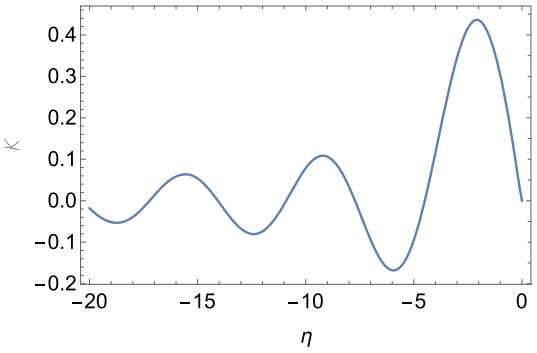

FIG. 7. Kernel $\mathcal{K}$ as a function of $\eta \equiv k\tau$.

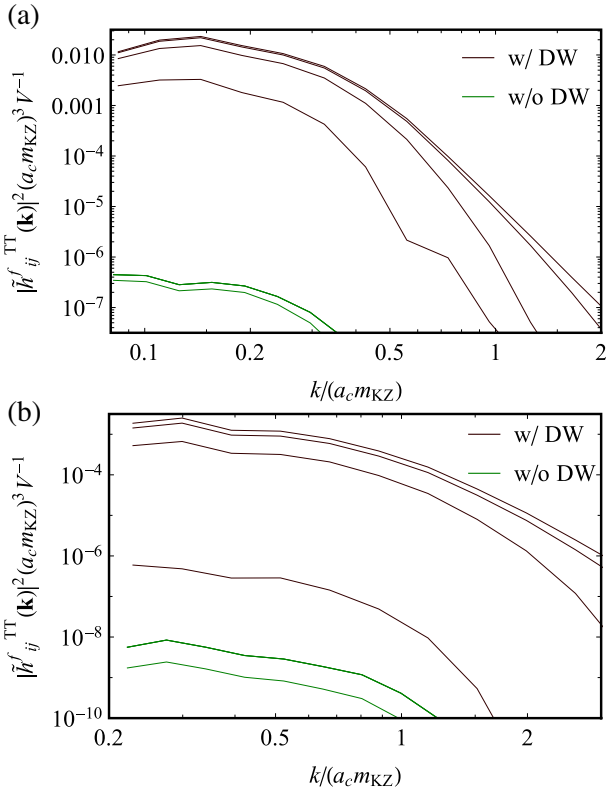

FIG. 8. Spectrum of $\langle|\tilde{h}_{ij}^f|^2\rangle$ for scenarios (A) (up) and (B) (down). The choices of parameters in the potential are the same as in Fig. 4. The spectrum is accumulated up to $\ln(a/a_c) = 1.3, 2.3, 3.3$, and 4.3. As a comparison, the spectrum without DW production is also shown by the green curves, where for both (A) and (B) the $\ln(a/a_c) = 2.3$, 3.3, 4.3 curves are identical, which indicates that the GW production ceases completely after $\ln(a/a_c) = 2.3$.

There are mainly two contributions to $\tilde{T}_{ij}^{TT}(\tau',\mathbf{k})$, namely, the fluctuations of the σ field and the DWs, which appear when the fluctuations cool down, as shown in Figs. 5 and 6. As we can see from Figs. 5 and 6, the amplitude of the small scale fluctuations becomes significantly smaller than the size of DWs at about two e-folds after the phase transition. However, we can can see from

Fig. 8 that between two and three e-folds after the phase transition, the GWs still grows significantly. Therefore, we can see that after about two e-folds the dominant source for GW production should be from the DWs.

To numerically compare the importance of the two contributions, we perform simulations without DW formations. To do this, we use the same parameters as in the simulations with DW formations to generate the initial configuration $\sigma(\mathbf{x})$ induced by the exponential growth. Then, we replace $\sigma(\mathbf{x})$ with $|\sigma(\mathbf{x})|$ for the initial condition of the nonlinear growth. This way, we eliminate all of the DWs while keeping the initial fluctuations of the σ field. The green curves in Fig. 8 show the accumulated $|\tilde{h}_{ij}|^2/V$ without DWs for both scenarios (A) and (B), in which the green curves for $\ln(a/a_c) = 2.3$, 3.3, 4.3 are identical in both scenarios. The coincidences indicate that without DWs, the GW production stops at about $\ln(a/a_c) = 2.3$ because the oscillations of σ are quickly damped by the Hubble expansion, as shown in Fig. 4. This also agrees with the result in [31]. From Eq. (8), one can also see that without DWs the GW spectra stop growing after about two e-folds, and the strengths are also significantly smaller compared to the case with DWs. Therefore, we can conclude that the DWs dominate the production of the GWs. In the next section, we provide semianalytical analyses for the size of the GW spectrum induced by both DWs and the fluctuations.

IV. SEMIANALYTICAL DERIVATION OF THE GW SIGNAL

In this section, we present a derivation to the size of the SGWB signal, discuss the IR and UV behavior of the SGWB spectrum, and compare the analytical result with numerical simulations.

Due to the shape of the kernel $\mathcal{K}$, as shown in Fig. 7, the dominant contribution of $\tilde{T}^{TT}_{ij}(\tau', \mathbf{k})$ to $\tilde{h}^f_{ij}(\mathbf{k})$ happens at $k\tau' \approx -2$. We only keep this dominant contribution to estimate the peak value of $\Omega_{\rm GW}$. Thus, we have

$$\frac{\langle|\tilde{h}^f_{ij}|^2\rangle}{V} = \mathcal{A}_2\left[\frac{16\pi G_N}{k^2}\right]^2 \frac{\langle|\tilde{T}^{TT}_{ij}(-2/k, \mathbf{k})|^2\rangle}{V}. \quad (28)$$

Here, $\langle\cdots\rangle$ means taking the average over the direction of $\mathbf{k}$.

The space average value of $T^{TT}(\tau, x)^2$ can be written as

$$\frac{1}{V}\int d^3x \tilde{T}^{TT}_{ij}(\tau, \mathbf{x})\tilde{T}^{TT}_{ij}(\tau, \mathbf{x}) = \frac{1}{V}\int \frac{d^3k}{(2\pi)^3}|\tilde{T}^{TT}_{ij}(\tau, \mathbf{k})|^2. \quad (29)$$

The largest correlation of the σ field after the phase transition is determined by $m_{\rm KZ}$, and the typical size of independent regions in the Universe is about $2\pi m^{-1}_{\rm KZ}$. Thus, to calculate the spatial integral in (29), we can first define a window function $W^{(a)}$ for each region. Each region's center position is at $\mathbf{x}^{(a)}$. Then, the energy-momentum tensor can be decomposed as

$$T^{TT}_{ij}(\tau, \mathbf{x}) = \sum_a (T^{TT}_{ij}(\tau, \mathbf{x})W^{(a)}(\mathbf{x})). \quad (30)$$

Then, we can define $\tilde{T}^{TT(a)}_{ij}(\tau, \mathbf{k})$ as

$$\tilde{T}^{TT(a)}_{ij}(\tau, \mathbf{k}) = \int d^3x T^{TT}_{ij}(\tau, \mathbf{x})W^{(a)}(\mathbf{x})e^{-i\mathbf{k}\cdot(\mathbf{x}-\mathbf{x}^{(a)})}. \quad (31)$$

Therefore, we have

$$\tilde{T}^{TT}_{ij}(\tau, \mathbf{k}) = \sum_a \tilde{T}^{TT(a)}_{ij}(\tau, \mathbf{k})e^{i\mathbf{k}\cdot\mathbf{x}^{(a)}}. \quad (32)$$

Then, the right-hand side of (29) can be written as

$$\frac{1}{V}\int \frac{d^3k}{(2\pi)^3}\sum_{a,b}\tilde{T}^{TT(a)}_{ij}(\tau, \mathbf{k})T^{TT(b)}_{ij}(\tau, \mathbf{k})^* e^{i\mathbf{k}\cdot(\mathbf{x}^{(a)}-\mathbf{x}^{(b)})}. \quad (33)$$

The interference contributed by different patches is suppressed. Therefore, it can be further simplified as

$$\frac{1}{V}\int \frac{4\pi k^3 d\ln k}{(2\pi)^3}\left\langle\sum_a|\tilde{T}^{TT(a)}_{ij}(\tau, \mathbf{k})|^2\right\rangle. \quad (34)$$

In comoving coordinates, the size of each independent region is about $2\pi m^{-1}_{\rm KZ}a_c^{-1}$. Therefore, the above expression can be simplified as

$$\mathcal{A}_3\left(\frac{m_{\rm KZ}a_c}{2\pi}\right)^3\int \frac{4\pi k^3 d\ln k}{(2\pi)^3}|\tilde{T}^{TT(A)}_{ij}(\tau, k)|^2, \quad (35)$$

where $\mathcal{A}_3$ is a numerical factor and $|\tilde{T}^{TT(A)}_{ij}(\tau, k)|^2$ can be seen as the space and angular averaged value of $|\tilde{T}^{TT(a)}_{ij}(\tau, \mathbf{k})|^2$.

Consider the DW contribution to $\tilde{T}^{TT}_{ij}$ in one region. $\tilde{T}^{TT}_{ij}(\tau, \mathbf{k})$ can be expressed as

$$\tilde{T}^{TT}_{ij}(\tau, \mathbf{k}) = \int \frac{d^3p}{(2\pi)^3}\Lambda_{ij,kl}p^k p^l\tilde{\sigma}(\mathbf{p})\tilde{\sigma}(\mathbf{k}-\mathbf{p}). \quad (36)$$

We know that the modes with $k \sim m_{\rm KZ}a_c$ dominate the contribution to the SGWB and, as we will see later, the p integral in (36) is dominated by the region $p \sim m \gg m_{\rm KZ}$. Therefore, we can neglect the $\mathbf{k}$ in $\tilde{\sigma}$ as a qualitative estimate. Then, the angular average of $\tilde{T}^{TT}_{ij}(\tau, \mathbf{k})\tilde{T}^{TT}_{ij}(\tau, \mathbf{k})$ contributed by a single region can be written as

$$\int \frac{d^3p}{(2\pi)^3}\int \frac{d^3q}{(2\pi)^3}\left[\int \frac{d\hat{\mathbf{k}}}{4\pi}\Lambda_{ij,kl}\Lambda_{ij,k'l'}p^k p^l q^{k'} q^{l'}\right] \times |\tilde{\sigma}(\mathbf{p})|^2|\tilde{\sigma}(\mathbf{q})|^2. \quad (37)$$

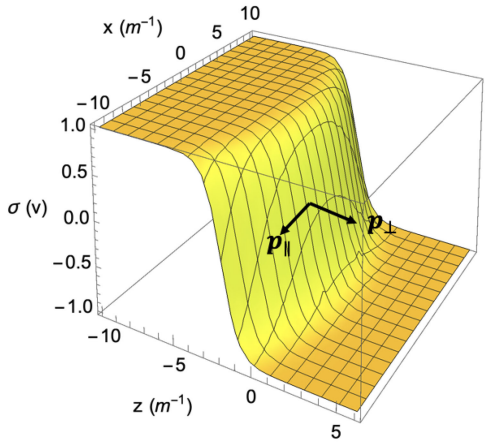

FIG. 9. Illustration of DW configuration.

A simple calculation gives

$$\int \frac{d\hat{\mathbf{k}}}{4\pi}\Lambda_{ij,kl}\Lambda_{ij,k'l'}p^k p^l q^{k'} q^{l'} = \frac{2}{5}(\mathbf{p}\cdot\mathbf{q})^2 - \frac{2}{15}p^2q^2.$$

A typical DW configuration is shown in Fig. 9, where we only present the space's x and z coordinates. We can decompose the comoving momenta $\mathbf{p}$ and $\mathbf{q}$ in Eq. (38) into the direction that is perpendicular to the surface of the wall (the z direction as in Fig. 9) and the directions that are parallel to the wall surface. For a generic DW, if we neglect its thickness, it can be seen as a Heaviside theta function. In our case, if we only consider the field configuration along the z direction, it can be written as

$$\sigma(z) = v(1 - 2\Theta(z)). \tag{38}$$

The Fourier transformation of the above configuration is

$$\tilde{\sigma}(p_z) = -\frac{iv}{\pi p_z}. \tag{39}$$

Therefore, we expect that, for a general configuration, $\tilde{\sigma}(\mathbf{p})$ has the form

$$\tilde{\sigma}(\mathbf{p},\tau) = \frac{\tilde{\sigma}_\parallel(\mathbf{p}_\parallel,\tau)}{p_\perp} \tag{40}$$

in the region where $m_{\rm KZ}a_c < p < d_w^{-1}a(\tau)$, where d_w is the physical wall thickness. As an example, in the Landau-Ginzburg type model, as discussed in this work, the DW configuration can be approximated as

$$\sigma(z) = v\tanh\left(\frac{mz}{\sqrt{2}}\right). \tag{41}$$

The Fourier transformation is

$$\tilde{\sigma}(p_z) = \frac{iv}{2^{1/2}m}\,\mathrm{csch}\left(\frac{\pi p_z}{\sqrt{2}m}\right). \tag{42}$$

Then, we know that for $p_z < m$, $\tilde{\sigma}(p_z)$ drops as p_z^{-1}, and for $p_z > m$, $\tilde{\sigma}(p_z)$ drops exponentially.

In the parallel directions, since the oscillations on the surface of the wall are quickly diluted by the expansion of the Universe, the configuration changes slowly. Therefore, we do not expect $\tilde{\sigma}_\parallel$ to have significant support for $p_\parallel > m_{\rm KZ}a_c^{-1}$. Now, we can decompose the $\mathbf{p}$ and $\mathbf{q}$ integrals in Eq. (38) into $d^2p_\parallel dp_\perp d^2q_\parallel dq_\perp$, and then it becomes

$$\int \frac{d^2\mathbf{p}_\parallel dp_\perp}{(2\pi)^3}\int \frac{d^2\mathbf{q}_\parallel dq_\perp}{(2\pi)^3}\left[\frac{2}{5}(\mathbf{p}_\parallel\cdot\mathbf{q}_\parallel + p_\perp q_\perp)^2 - \frac{2}{15}(p_\parallel^2 + p_\perp^2)(q_\parallel^2 + q_\perp^2)\right]\frac{|\tilde{\sigma}_\parallel(\mathbf{p}_\parallel)|^2}{p_\perp^2}\frac{|\tilde{\sigma}_\parallel(\mathbf{q}_\parallel)|^2}{q_\perp^2}, \tag{43}$$

where the $p_\perp$ and $q_\perp$ integrals are from $m_{\rm KZ}$ to $d_w^{-1}a(\tau)$. From (43) one can see that the $p_\perp$ and $q_\perp$ integrals are dominated in the region $p_\perp \sim d_w^{-1}a(\tau)$ and $q_\perp \sim d_w^{-1}a(\tau)$, whereas the supports of the $p_\parallel$ and $q_\parallel$ integrals are around $m_{\rm KZ}a_c$. Thus, when we estimate the value of (43), we can use the approximation $p_\parallel, q_\parallel \ll p_\perp, q_\perp$. Another thing to notice is that $\tilde{\sigma}$ must be proportional to $v_{\rm temp}$, the temporary vacuum expectation value of the σ field. Then, (43) can be estimated as

$$\mathcal{A}_4 \times \frac{d_w^{-2}a^2(\tau)v_{\rm temp}^4}{[m_{\rm KZ}a_c]^4}, \tag{44}$$

where $[m_{\rm KZ}a_c^{-1}]^4$ in the denominator is from dimensional analysis and $\mathcal{A}_4$ collects all of the numerical factors when calculating the integral.

Figure 10 shows $|\tilde{T}_{ij}^{TT}|^2$ at different times after the phase transition. One can see that the distributions are flat for small k, and drop as $k^{-3} \sim k^{-4}$ when $k > m_{\rm KZ}a_c$.

Together with (25), (28), (35), (44), and $a(\tau = -2/k) = k/(2H)$, we arrive at

$$\frac{d\rho_{\rm GW}}{d\ln k} = \mathcal{A}_1\frac{G_N|\mathcal{E}_0^i|^2k^3}{H^2(m_{\rm KZ}a_c)a^4}\frac{v_{\rm temp}^4}{d_w^2}, \tag{45}$$

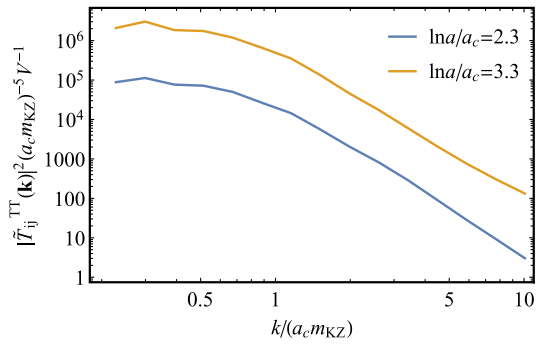

FIG. 10. $|\tilde{T}_{ij}^{TT}|^2$ at different times as a function of k.

where $\mathcal{A}_1$ collects all of the numerical factors. Now, let us focus on the case where reheating happens fast and finishes within one e-fold. Then, as shown in [45],

$$\mathcal{E}_0^i = \frac{a_{\rm end}^2 H}{k}, \tag{46}$$

where $a_{\rm end}$ is the scale factor at the end of inflation. Thus, in the RD era we have

$$\frac{d\rho_{\rm GW}}{d\ln k} = \mathcal{A}_1 \frac{G_N k}{m_{\rm KZ} a_c} \frac{v_{\rm temp}^4}{d_w^2} \left(\frac{a_{\rm end}}{a}\right)^4. \tag{47}$$

In the instantaneous reheating case, neglecting the change in the number of relativistic degrees of freedom, the radiation energy density can be written as

$$\rho_R = \frac{3H^2}{8\pi G_N} \left(\frac{a_{\rm end}}{a}\right)^4. \tag{48}$$

Thus, we have

$$\Omega_{\rm GW} = \Omega_R \mathcal{A}_1 \frac{8\pi G_N^2 k}{3H^2 m_{\rm KZ} a_c} \frac{v_{\rm temp}^4}{d_w^2}. \tag{49}$$

In Landau-Ginzburg type model, as shown in Eq. (3), we have

$$d_w \sim m_{\rm temp}^{-1}, \qquad \Delta\rho = \frac{m_{\rm temp}^4}{\lambda}, \qquad v_{\rm temp}^2 = \frac{m_{\rm temp}^2}{\lambda}. \tag{50}$$

Therefore, we have

$$\Omega_{\rm GW} = \Omega_R \mathcal{A}_1 \frac{8\pi G_N^2 k}{3H^2 m_{\rm KZ} a_c} \Delta\rho^2 d_w^2. \tag{51}$$

During inflation, we have

$$H^2 = \frac{8\pi G_N \rho_{\rm inf}}{3}. \tag{52}$$

Then, we have

$$\Omega_{\rm GW} = \Omega_R \mathcal{A}_1 \frac{3}{8\pi} \frac{k}{m_{\rm KZ} a_c} \left(\frac{\Delta\rho}{\rho_{\rm inf}}\right)^2 H^2 d_w^2. \tag{53}$$

This result assumes that $k \ll m a_c$; thus, we can neglect the k dependence in $\tilde{\sigma}$ when calculating $|\tilde{T}_{ij}^{TT}|^2$. However, we see in Fig. 10 that $|\tilde{T}_{ij}^{TT}|^2$ drops significantly when $k > m_{\rm KZ} a_c$. Therefore, the peak position of $\Omega_{\rm GW}$ is around $k = m_{\rm KZ} a_c$, and we arrive at the formula

$$\Omega_{\rm GW}^{\rm peak} = \Omega_R \mathcal{A} (H d_w)^2 \left(\frac{\Delta\rho}{\rho_{\rm inf}}\right)^2, \tag{54}$$

where $\mathcal{A}$ collects all of the numerical factors.

For scenario (A), as shown in Fig. 4, $v_{\rm temp}$ arrives at $m\lambda^{-1/2}$ within about one e-fold after the critical time. Thus, to estimate $\Omega_{\rm GW}$ we can use the parameters in the Lagrangian. However, for scenario (B), $v_{\rm temp}$ changes slowly with ϕ_0 after the phase transition. Therefore, to have an empirical formula for $\Omega_{\rm GW}^{\rm peak}$ for scenario (B), we take $\tau = -2/(m_{\rm KZ} a_c)$ to evaluate d_w and $\Delta\rho$.

A byproduct of (53) is that it predicts that on the left side of the peak, $\Omega_{\rm GW}$ increases as k^1 until it reaches the peak. For $k \ll m_{\rm KZ} a_c$, from a causality argument, we have $\Omega_{\rm GW} \sim k^3$ [54]. Thus, Eq. (53) predicts that there is a transition of $\Omega_{\rm GW}$ from k^3 to k^1 before reaching the peak frequency. This behavior is clearly shown by the numerical simulation presented in Fig. 11. The k^1 behavior before reaching the peak can be seen as a nontrivial check of the numerical simulation.

The analytical formula (54) also shows that $\Omega_{\rm GW}^{\rm peak}$ is proportional to H^2. This is also confirmed by the numerical simulations. In Fig. 12, we show $\Omega_{\rm GW}^{\rm peak}$ as a function of

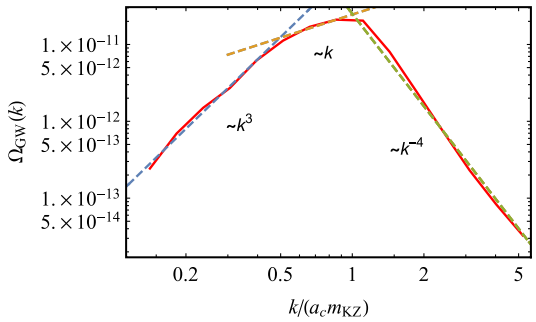

FIG. 11. Qualitative behavior of the GW spectrum. Here, we assume that the modes reentered the horizon during the RD era. In the far IR region, $\Omega_{\rm GW}$ increases as k^3 and then transits into k^1 when approaching the peak. Then, it decays as k^{-4} in the UV region.

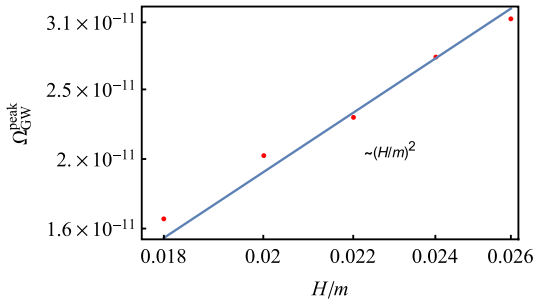

FIG. 12. Qualitative behavior of the GW spectrum. We plot $\Omega_{\rm GW}^{\rm peak}$ as a function of H/m.

H/m. We can see clearly that the qualitative behavior shown in (54) is correct.

As a comparison, we present here a semianalytic estimation of the size of the GW spectrum with the DW production turned off by replacing $\sigma(x)$ with $|\sigma(x)|$. Then, the GW production process is similar to case of GW production during preheating [31]. The fluctuations around the temporary vacuum can be described by a series of plane waves with typical comoving momentum $a_c m_{\rm KZ}$, where a_c is the scale factor at the phase transition. Thus, the size of the gradient part of the energy-momentum tensor can be estimated as

$$|T_{ij}| = |\partial_i\sigma\partial_j\sigma| \simeq a_c^2 m_{\rm KZ}^2 v_{\rm temp}^2. \tag{55}$$

Generically, $T^{\rm TT}$ is much smaller than the trace part of T_{ij}, and we can write

$$|T_{ij}^{TT}| = \alpha|T_{ij}|, \tag{56}$$

where α is about 0.1 [55]. Then, the peak value of $|\tilde{T}_{ij}^{TT}|$, the Fourier transform of $T^{\rm TT}$, can be estimated as

$$|\tilde{T}_{ij}^{TT}|_{\rm peak} \simeq (a_c m_{\rm KZ})^{-3}|T_{ij}^{TT}|. \tag{57}$$

Then, from Eq. (26), h^f, the tensor perturbation frozen onto the horizon, can be written as

$$|\tilde{h}_{ij}^f|_{\rm peak} \simeq 16\pi G_N \frac{H}{a_c^2 m_{\rm KZ}^2}|\tilde{T}_{ij}^{TT}|_{\rm peak}\Delta t, \tag{58}$$

where we only keep the leading term in the kernel $\mathcal{K}$. In Eq. (58), $\Delta t \simeq 10 m_{\rm temp}^{-1}$ is the typical time scale of those fluctuations [31]. Together with (28) and (44), we have

$$\frac{|\tilde{h}_{ij}^f|^2_{\rm w/o\,DW}}{|\tilde{h}_{ij}^f|^2_{\rm w/DW}} \simeq \mathcal{B}(Hd_w)^4 = 10^{-6}, \tag{59}$$

where $\mathcal{B} = \mathcal{A}_4^{-1}(10\alpha)^2$ is a numerical factor. We can see that the ratio is parametrically small since $Hd_w \ll 1$, which agrees with the Fig. 8.

V. EVOLUTION OF THE UNIVERSE BETWEEN INFLATION AND REHEATING

After inflation, the Universe might undergo an intermediate stage before the RD era. The GW modes may reenter the horizon in the intermediate stage, and then the spectrum will be distinct. Generally, the scale factor can be parametrized as $a(t) \sim t^p$, with $p < 1$. Using conformal time, the scale factor of the intermediate stage can be written as

$$a = a_{\rm end}\left(\frac{\tau}{\tau_{\rm end}}\right)^{\frac{p}{1-p}}, \tag{60}$$

where the subscript "end" denotes the end of inflation. Then, in the intermediate stage $\tilde{h}_{ij}$ satisfies

$$\tilde{h}_{ij}''(\tau,\mathbf{k}) + \frac{p}{1-p}\frac{2}{\tau}\tilde{h}_{ij}'(\tau,\mathbf{k}) + k^2\tilde{h}_{ij}(\tau,\mathbf{k}) = 0. \tag{61}$$

For the modes to reenter the horizon, the initial conditions can be written as

$$\tilde{h}_{ij}(\tau_{\rm end},\mathbf{k}) = h_{ij}^f(\mathbf{k}), \qquad \tilde{h}_{ij}'(\tau_{\rm end},\mathbf{k}) = 0. \tag{62}$$

The exact solution of this equation can be expressed as

$$\tilde{h}_{ij}(\tau,\mathbf{k}) = \Gamma[1-\nu]\left(\frac{k\tau}{2}\right)^{\nu}[\cos\nu\pi J_\nu(k\tau) - \sin\nu\pi Y_\nu(k\tau)]\tilde{h}_{ij}^f(\mathbf{k}), \tag{63}$$

where J_ν, Y_ν are the Bessel functions with

$$\nu = \frac{3}{2} + \frac{1}{p-1}. \tag{64}$$

When the universe enters the RD era, $\tilde{h}_{ij}$ satisfies

$$\tilde{h}_{ij}''(\tau,\mathbf{k}) + \frac{2}{\tau}\tilde{h}_{ij}'(\tau,\mathbf{k}) + k^2\tilde{h}_{ij}(\tau,\mathbf{k}) = 0.$$

We match $\tilde{h}$ and $\tilde{h}'$ at the transition time between the intermediate stage and the RD era to get the initial conditions. Then, the general form for $\tilde{h}_{ij}$ can be written as

$$\tilde{h}_{ij}(\tau,\mathbf{k}) = \frac{A}{k\tau}[S\cos(k\tau) + C\sin(k\tau)]\tilde{h}_{ij}^f(\mathbf{k}).$$

Here,

$$A = \frac{1}{\frac{1}{2}-\nu}\frac{\Gamma[1-\nu]}{2^{\nu-\frac{1}{2}}\sqrt{\pi}}x^{\frac{1}{2}+\nu}, \tag{65}$$

$$S = \cos\left(\frac{x}{\frac{1}{2}-\nu}\right)\sqrt{\frac{\pi}{2}x}[\cos\nu\pi J_\nu(x) - \sin\nu\pi Y_\nu(x)] - \sin\left(\frac{x}{\frac{1}{2}-\nu}\right)\sqrt{\frac{\pi}{2}x}\left[\cos\nu\pi\left(J_\nu'(x) + \frac{1}{2x}J_\nu(x)\right) - \sin\nu\pi\left(Y_\nu'(x) + \frac{1}{2x}Y_\nu(x)\right)\right], \tag{66}$$

$$C = \sin\left(\frac{x}{\frac{1}{2}-\nu}\right)\sqrt{\frac{\pi}{2}x}[\cos\nu\pi J_\nu(x) - \sin\nu\pi Y_\nu(x)] + \cos\left(\frac{x}{\frac{1}{2}-\nu}\right)\sqrt{\frac{\pi}{2}x}\left[\cos\nu\pi\left(J_\nu'(x) + \frac{1}{2x}J_\nu(x)\right) - \sin\nu\pi\left(Y_\nu'(x) + \frac{1}{2x}Y_\nu(x)\right)\right], \tag{67}$$

with

$$x = \left(\frac{1}{2} - \nu\right)\left(\frac{a_{\rm re}}{a_{\rm end}}\right)^{\frac{1}{\frac{1}{2}-\nu}} \frac{k}{a_{\rm end}H_{\rm inf}}, \tag{68}$$

where $a_{\rm re}$ is the scale factor at the transition between the intermediate stage and the RD era. The x parameter here can be seen as the ratio between the physical momentum of the mode and the Hubble expansion rate at the transition between the intermediate stage and the RD era. Thus, $x > 1$ means that the modes reenter the horizon in the intermediate stage, and $x < 1$ means that the modes reenter the horizon after the intermediate stage.

Then, the GW energy density in the RD era can be written as

$$\frac{d\rho_{\rm GW}}{d\ln k} = \left(\frac{a_{\rm re}}{a_{\rm end}}\right)^{-\frac{1+2\nu}{\frac{1}{2}-\nu}} A^2(|S|^2 + |C|^2)\frac{d\rho_{\rm GW}}{d\ln k}\bigg|_{\rm IRH}, \tag{69}$$

where the subscript "IRH" stands for instantaneous reheating. On the other hand, with the nontrivial intermediate stage, the evolution of the total energy density of the Universe is also different. By simply counting the redshifts after reheating, the energy density of radiation can be written as

$$\rho_R = \left(\frac{a_{\rm re}}{a_{\rm end}}\right)^{-\frac{1+2\nu}{\frac{1}{2}-\nu}} \rho_R|_{\rm IRH}. \tag{70}$$

Thus, we have

$$\Omega_{\rm GW}(k) = D(k)\Omega_{\rm GW}(k)|_{\rm IRH}, \tag{71}$$

where

$$D(k) = A^2(|S|^2 + |C|^2). \tag{72}$$

One can see that an intermediate stage can change both the shape and strength of the GW signal. The distortion factor D satisfies

$$D(k) = 1, \qquad x \ll 1, \tag{73}$$

$$D(k) = A^2, \qquad x \gg 1. \tag{74}$$

In Fig. 13, we show the distortion functions for matter domination (MD) and kination domination (KD) intermediate stage separately. In the $x \gg 1$ limit, the mode reenters the horizon during the intermediate stage. Then we have

$$\text{MD: } D(k) = \frac{9}{16}\left(\frac{a_{\rm re}}{a_{\rm end}}\right)^{-1}\left(\frac{k}{a_{\rm end}H_{\rm inf}}\right)^{-2} = \frac{9}{16}z_{\rm mp}^{-1}, \tag{75}$$

$$\text{KD: } D(k) = \frac{4}{\pi}\left(\frac{a_{\rm re}}{a_{\rm end}}\right)^{2}\frac{k}{a_{\rm end}H_{\rm inf}} = \frac{4}{\pi}z_{\rm mp}^{2}, \tag{76}$$

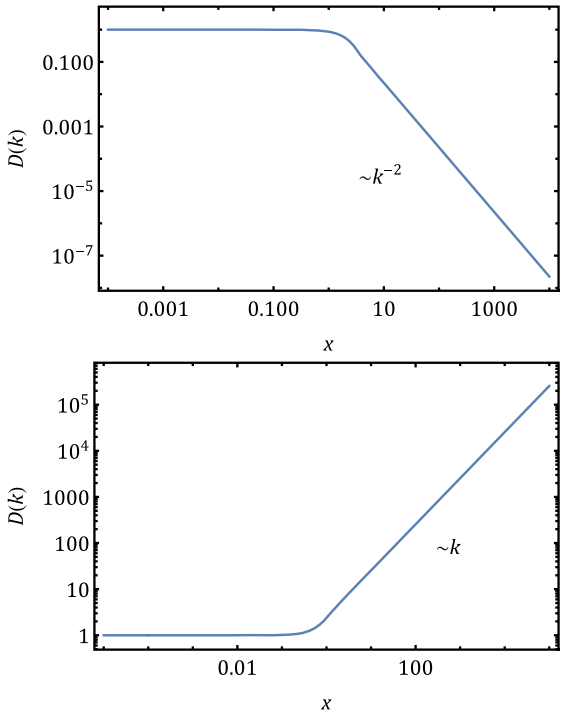

FIG. 13. Distortion function $D(k)$ as a function of x for the MD intermediate stage (top) and KD intermediate stage (bottom), respectively.

where $z_{\rm mp}$ is the redshift from the mode that reenters the horizon to the end of the intermediate stage.

VI. DETECTABILITY OF THE GW SIGNAL

Today's GW relative abundance can be calculated from Eq. (25),

$$\Omega_{\rm GW}(f) = \Omega_R \times \rho_R^{-1}\frac{d\rho_{\rm GW}}{d\ln f}\bigg|_{\rm today}, \tag{77}$$

where Ω_R and ρ_R are today's radiation abundance and energy density. $f = k/(2\pi a_{\rm today})$ gives today's GW frequency. The detailed shape of $\Omega_{\rm GW}(f)$ also depends on the Universe's evolution when the GW modes reenter the horizon. From the end of inflation to the completion of reheating, the Universe may undergo transition eras, such as MD and KD [56,57]. As shown in Sec. V (see also [45]), the peak value of $\Omega_{\rm GW}(f)$ is not sensitive to the Universe's evolution when the modes are outside the horizon. During KD, the total energy density of the Universe drops as a^{-6}, whereas the energy density of GWs drops as a^{-4}, and therefore $\Omega_{\rm GW}(f)$ gets a relative enhancement [58,59]. On the other hand, if the GW modes reenter the horizon in an intermediate MD era before reheating, the total energy of the Universe drops as a^{-3}. Thus, in this case $\Omega_{\rm GW}$ obtains a relative suppression. Therefore, the detailed GW spectrum also strongly depends on N_k and N_m, the numbers of

TABLE I. Values of $\mathcal{A}$ together with α for different scenarios and intermediate stages before reheating.

$\mathcal{A}$	IRH	MD ($\alpha=-1$)	KD ($\alpha=2$)
Scenario A	0.15	0.09	0.2
Scenario B	0.3	0.15	0.3

e-folds during the KD and MD intermediate stages, respectively. Explicitly, we have

$$N_{k,m}=\ln(a_{\rm re}/a_{\rm end}). \tag{78}$$

From qualitative arguments and numerical simulations presented in Sec. IV, we can derive a semianalytical formula for the peak value of $\Omega_{\rm GW}$,

$$\Omega_{\rm GW}^{\rm peak}=\Omega_R\times\mathcal{A}(Hd_w)^2\times\left(\frac{\Delta\rho}{\rho_{\rm inf}}\right)^2 z_{\rm mp}^{\alpha}, \tag{79}$$

where d_w is the physical wall thickness at $\tau=-2/m_{\rm KZ}$ and $z_{\rm mp}$ is defined in Eq. (75) and measures the redshift of the Universe between the time that the peak mode reenters the horizon and the end of the intermediate stage. Table I presents the values of $\mathcal{A}$ and α for scenarios (A) and (B) and for different intermediate stages before reheating.

Future GW detectors will be able to detect SGWB produced during inflation by the DWs. Figure 14 shows today's SGWB spectra and the sensitivities of PTAs and space- and ground-based GW telescopes. Here we consider scenario (B), and the parameters for the spectator sector and inflaton model are the same as for the lower panel of Fig. 8. We consider three after-inflation-evolution scenarios: instantaneous reheating, intermediate MD, and intermediate KD. As shown in Fig. 14, for $N_c\approx 40$ the SGWB spectrum falls within the region of PTAs, and it is possible to use it to explain the common noise process. For $N_c\approx 20$–25, the SGWB can be detected by the planned space-based GW detectors such as LISA, Taiji, and TianQin. For $N_c\approx 10$, it can be seen by future terrestrial GW detectors.

If $N_c\approx 60$, the GW frequency can be about 10^{-19} Hz and can be detected via the CMB B-mode spectrum. Here we consider scenario (A), in which the backreaction to the curvature perturbation will not ruin the temperature correlation in the CMB spectrum [43]. With reasonable choices of parameters, as shown in Fig. 15, the future CMB-S4 experiment will be able to detect the signal. Furthermore, we can also see that the shape of the B-mode spectrum induced by the phase transition differs from the quantum-induced one. Therefore, future CMB observations will be able to distinguish the origin of the SGWB source.

We have already seen from previous discussions that the GW signal can be enhanced by the KD intermediate stage. However, a long intermediate stage will postpone reheating and thus significantly lower the reheating temperature. Therefore, we expect an upper bound on the enhancement factor $D(k)$ in Eqs. (71) and (76). Assuming that reheating happens right after the end of the KD era, we have

$$3H_{\rm inf}^2M_{\rm pl}^2e^{-6N_k}=\frac{\pi^2}{30}g_\star T_{\rm RH}^4. \tag{80}$$

Substituting the above equation into $D(k)$ in Eq. (76), we have for KD

$$\begin{aligned}D(k)&=\frac{12\sqrt{10}}{\pi^2}g_\star^{-1/2}\frac{M_{\rm pl}}{T_{\rm CMB}}\frac{2\pi f_{\rm today}}{T_{\rm RH}}\left(\frac{g_{\star S}}{g_{\star S0}}\right)^{1/3}\\&\approx 10^3\times\left(\frac{f_{\rm today}}{10^{-8}\ {\rm Hz}}\right)\left(\frac{T_{\rm RH}}{1\ {\rm MeV}}\right)^{-1},\end{aligned} \tag{81}$$

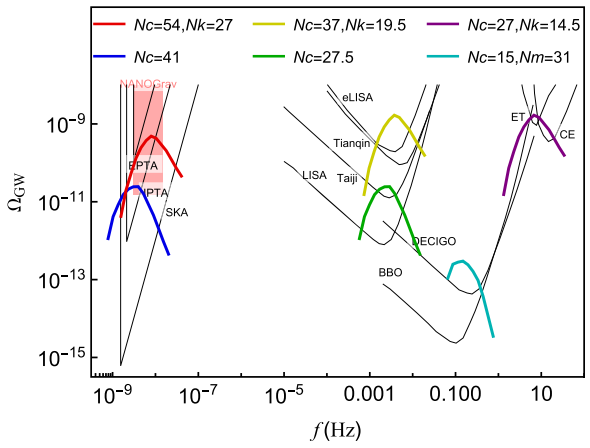

FIG. 14. Spectra of today's SGWB energy density distribution for scenario (B), together with the sensitivity curves of future GW detectors and the region favored by the NanoGrav observation. In the plot, N_c is the number of e-folds from the critical point to the end of inflation, and N_k and N_m are the number of e-folds during the intermediate KD and MD, respectively.

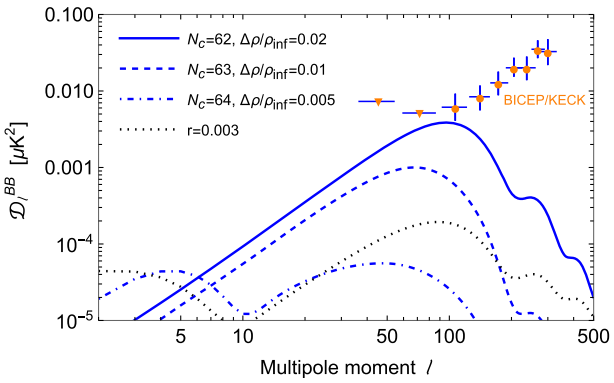

FIG. 15. B-mode power spectra induced by the SGWB in scenario (A) for different choices of phase transition time and potential energy in the spectator sector. As a comparison, the B-mode spectrum generated via tensor-mode quantum fluctuations with a tensor-scalar ratio $r=0.003$ is also shown. The orange dots and triangles are for the data from the BICEP/KECK array.

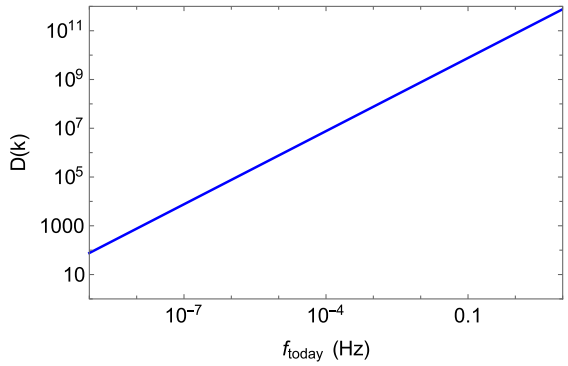

FIG. 16. Upper limit on the enhancement factor $D(k)$ as a function of today's GW frequency.

where $g_\star$ is the total number of effectively massless degrees of freedom at reheating, and $g_{\star S}$ and $g_{\star S0}$ are the total number of effectively massless degrees of freedom to calculate the entropy density at reheating and today, respectively. We can see that the Hubble parameter does not appear in $D(k)$. Successful big bang nucleosynthesis requires $T_{\rm RH} > 1$ MeV, and the upper limit on $D(k)$ is plotted in Fig. 16. We can see that the KD intermediate region can bring an $\mathcal{O}(10^3)$ enhancement for PTA-frequency GW signals. For $\mathcal{O}(10^{-3})$ Hz GW signals, the enhancement can be as large as 10^8. In Fig. 14, the red, yellow, and purple curves show the cases in which a KD intermediate stage is considered between inflation and reheating. If such an enhancement exists, the SGWB signal is more likely to be measured by future detectors.

VII. SUMMARY AND DISCUSSIONS

In this work, we numerically studied the SGWB produced by second-order phase transitions during inflation accompanied by a spontaneous breaking of a Z_2 symmetry. We found that the most essential contribution to GW production is from DWs. We show this in three ways.

(1) From Figs. 5 and 6, we can see that fluctuations of the σ field around the minima become significantly decreased from $a/a_c = 2.3$ to 3.3. However, as shown in Fig. 8, from $a/a_c = 2.3$ to 3.3, $|h^{fTT}|^2$ still increases significantly.

(2) To show that the DW structure dominates the GW production, we turned off the DW production by setting $\sigma \to |\sigma|$ before the nonlinear evolution. In this way, we extinguished the topological structure, leaving the fluctuations around the minima roughly unchanged. The green curves in Fig. 8 show the results. We can see that without DWs, the GW production stops at about two e-folds after the critical time, and the size of the GW signal is about 5 orders of magnitude smaller than the case with DWs.

(3) In Sec. IV we did a qualitative analysis of the size and shape of the GW spectrum, assuming only the DW contribution. In this analysis, as shown in Eq. (54) and Fig. 11, we found that both the qualitative size and the shape of the GW spectrum agree with the numerical simulation.

Thus, we have shown that, due to the severe violation of the time-translation symmetry during inflation, even the cosmologically static DW configurations, without forming a network, can create detectable SGWB for future GW detectors. We also showed that with the KD intermediate stage the SGWB produced in scenarios can be used to explain the common red noise observed by NanoGrav.

This work emphasized the DW-induced SGWB during inflation. We assumed that the DWs decay sufficiently fast, so the DW network disappears before dominating the Universe. We leave the discussions of the fate of DWs and their phenomenological consequences to future studies.

Scenario (A) discussed in this work may also be realized in warm inflation models, where the decay of the inflaton field supports the thermal plasma [60,61]. In scenario (B), the interaction between the ϕ and σ leads to a backreaction to curvature perturbations, and the Lagrangian can be written as $y\sigma^2\phi_0\delta\phi$. This term may induce secondary GWs once the induced curvature perturbations reenter the horizon. This term may also lead to the production of primordial black holes. We leave these interesting phenomena to future studies.

ACKNOWLEDGMENTS

We thank Lian-Tao Wang and Zhong-Zhi Xianyu for their helpful discussions. This work is supported in part by the National Key R&D Program of China under Grants No. 2021YFC2203100 and No. 2017YFA0402204, the NSFC under Grant No. 11975134, and the Tsinghua University Dushi Program No. 53120200422.

APPENDIX: DETAILS OF THE NUMERICAL SIMULATION

In this appendix, we present the algorithm of our numerical simulation.

The evolution of classical systems can be described by the Hamiltonian equations,

$$\sigma' = \frac{\delta \mathscr{H}}{\delta \pi} = \{\sigma, \mathscr{H}\}, \tag{A1}$$

$$\pi' = -\frac{\delta \mathscr{H}}{\delta \sigma} = \{\pi, \mathscr{H}\}, \tag{A2}$$

with the Poisson bracket $\{,\} \equiv \int d^3x \frac{\delta}{\delta\sigma}\frac{\delta}{\delta\pi} - \frac{\delta}{\delta\pi}\frac{\delta}{\delta\sigma}$. Defining $\mathcal{D}_{\mathscr{H}} = \{\cdot, \mathscr{H}\}$, the solutions of the Hamiltonian equations are

$$\sigma(\tau) = e^{\int \mathcal{D}_{\mathscr{H}} d\tau}\sigma(\tau_0), \tag{A3}$$

$$\pi(\tau) = e^{\int \mathcal{D}_{\mathscr{H}} d\tau}\pi(\tau_0). \tag{A4}$$

It is convenient to use the dimensionless variables

$$\Sigma = \frac{\sigma}{v}, \qquad \Pi = \frac{1}{m}\frac{\pi}{v}, \qquad M_{\rm eff} = \frac{m_{\rm eff}}{m},$$
$$X = mx, \qquad T = m\tau. \tag{A5}$$

Then, we have

$$\Sigma(T) = e^{\int \mathcal{D}_{\mathscr{H}/m} dT}\Sigma(T_0), \tag{A6}$$

$$\Pi(T) = e^{\int \mathcal{D}_{\mathscr{H}/m} dT}\Pi(T_0). \tag{A7}$$

For the case studied in this work, the Hamiltonian can be divided into two parts,

$$\mathscr{H} = \mathscr{K} + \mathscr{V}, \tag{A8}$$

with

$$\mathscr{K} = \frac{m}{\lambda}\int d^3\mathbf{X}\frac{1}{2}a^{-2}\Pi^2, \tag{A9}$$

$$\mathscr{V} = \frac{m}{\lambda}\int d^3\mathbf{X}\frac{1}{2}a^2\left(\frac{\partial\Sigma}{\partial\mathbf{X}}\right)^2 + a^4\left(\frac{1}{2}M_{\rm eff}^2\Sigma^2 + \frac{1}{4}\Sigma^4\right). \tag{A10}$$

We use the symplectic integrator method [62,63] to calculate the evolution of Σ numerically. We define

$$\mathscr{A} = \Delta T^{-1}\int_T^{T+\Delta T}\mathcal{D}_{\mathscr{K}/m}dT, \tag{A11}$$

$$\mathscr{B} = \Delta T^{-1}\int_T^{T+\Delta T}\mathcal{D}_{\mathscr{V}/m}dT. \tag{A12}$$

Here, the infinitesimal evolutions $\mathscr{A}$ and $\mathscr{B}$ are generated by the dimensionless kinetic energy potential energies $\mathscr{K}/m$ and $\mathscr{V}/m$. An nth-order symplectic integrator is defined as a symplectic approximation of the evolution operator with a difference of order $\mathcal{O}(\Delta T^{n+1})$,

$$e^{\int \mathcal{D}_{\mathscr{H}/m}dT} = e^{(\mathscr{A}+\mathscr{B})\Delta T} = \prod_{i=1}^{k} e^{c_i\mathscr{A}\Delta T}e^{d_i\mathscr{B}\Delta T} + \mathcal{O}(\Delta T^{n+1}), \tag{A13}$$

where $k = 8$ for the sixth-order accuracy used in this work. In our simulation, we use Solution A of the sixth-order symplectic integrator proposed in [63], and the values for the coefficients are

$$d_1 = d_7 = 0.784513610477560, \tag{A14}$$

$$d_2 = d_6 = 0.235573213359357, \tag{A15}$$

$$d_3 = d_5 = -1.17767998417887, \tag{A16}$$

$$d_4 = 1 - 2(d_1 + d_2 + d_3), \qquad d_8 = 0, \tag{A17}$$

$$c_1 = c_8 = \frac{d_1}{2}, \qquad c_2 = c_7 = \frac{d_1 + d_2}{2}, \tag{A18}$$

$$c_3 = c_6 = \frac{d_2 + d_3}{2}, \qquad c_4 = c_5 = \frac{d_3 + d_4}{2}. \tag{A19}$$

On the lattice, derivatives are replaced by differences. We use the neutral differential defined as

$$\Delta_x f(n) = \frac{8[f(n+1) - f(n-1)] - [f(n+2) - f(n-2)]}{12\delta x}.$$

The Laplacian is defined as

$$\Delta_x^2 f(n) = \frac{16[f(n+1) + f(n-1)] - [f(n+2) + f(n-2)] - 30f(n)}{12\delta x^2}. \tag{A20}$$

Both Δ_x and Δ_x^2 are at $\mathcal{O}(\delta x^4)$ accuracy. $\Delta_x f(n)$ can be written in the general form

$$\Delta_x f(n) = \frac{1}{\delta x}\sum_m \mathcal{D}(n-m)f(m), \tag{A21}$$

and in our case we have

$$\mathcal{D}(n) = \frac{8(\delta_{n,-1} - \delta_{n,1}) - (\delta_{n,-2} - \delta_{n,2})}{12}. \tag{A22}$$

With $\mathcal{D}(n)$ we can define the effective momentum,

$$k_{\tilde{n}}^{\rm eff} = \mathrm{i}\sum_m \frac{1}{\delta x}\mathcal{D}(m)e^{-\mathrm{i}\frac{2\pi}{N}\tilde{n}m}. \tag{A23}$$

Then, we define the transverse projective operator as [64,65]

$$\mathcal{P}_{ij}(\tilde{\mathbf{n}}) = \delta_{ij} - k_i^{\rm eff}(\tilde{\mathbf{n}})k_j^{\rm eff}(\tilde{\mathbf{n}})/|\mathbf{k}^{\rm eff}(\tilde{\mathbf{n}})|^2 \tag{A24}$$

to suppress the unphysical modes in the lattice calculation of the GWs. Specifically, in our choice of $\mathcal{D}(n)$ in (A22) we have

$$k_{\tilde{n}}^{\rm eff} = \frac{1}{\delta x}\left(\frac{4}{3}\sin\left[\frac{2\pi}{N}\tilde{n}\right] - \frac{1}{6}\sin\left[\frac{4\pi}{N}\tilde{n}\right]\right). \tag{A25}$$

[1] B. P. Abbott *et al.* (LIGO Scientific and Virgo Collaborations), Observation of gravitational waves from a binary black hole merger, Phys. Rev. Lett. **116**, 061102 (2016).

[2] R. Caldwell *et al.*, Detection of early-universe gravitational-wave signatures and fundamental physics, Gen. Relativ. Gravit. **54**, 156 (2022).

[3] P. A. Seoane *et al.* (eLISA Collaboration), The gravitational Universe, arXiv:1305.5720.

[4] P. Amaro-Seoane *et al.* (LISA Collaboration), Laser Interferometer Space Antenna, arXiv:1702.00786.

[5] S. Kawamura *et al.*, The Japanese space gravitational wave antenna: DECIGO, Classical Quantum Gravity **28**, 094011 (2011).

[6] J. Luo *et al.* (TianQin Collaboration), TianQin: A space-borne gravitational wave detector, Classical Quantum Gravity **33**, 035010 (2016).

[7] W.-H. Ruan, Z.-K. Guo, R.-G. Cai, and Y.-Z. Zhang, Taiji program: Gravitational-wave sources, Int. J. Mod. Phys. A **35**, 2050075 (2020).

[8] J. Crowder and N. J. Cornish, Beyond LISA: Exploring future gravitational wave missions, Phys. Rev. D **72**, 083005 (2005).

[9] G. Harry, P. Fritschel, D. Shaddock, W. Folkner, and E. Phinney, Laser interferometry for the big bang observer, Classical Quantum Gravity **23**, 4887 (2006); Classical Quantum Gravity **23**, 7361(E) (2006).

[10] V. Corbin and N. J. Cornish, Detecting the cosmic gravitational wave background with the big bang observer, Classical Quantum Gravity **23**, 2435 (2006).

[11] M. Kramer and D. J. Champion, The European Pulsar Timing Array and the Large European Array for pulsars, Classical Quantum Gravity **30**, 224009 (2013).

[12] A. Abramovici *et al.*, LIGO: The laser interferometer gravitational wave observatory, Science **256**, 325 (1992).

[13] F. Acernese *et al.* (Virgo Collaboration), Advanced Virgo: A second-generation interferometric gravitational wave detector, Classical Quantum Gravity **32**, 024001 (2015).

[14] M. Punturo *et al.*, The Einstein Telescope: A third-generation gravitational wave observatory, Classical Quantum Gravity **27**, 194002 (2010).

[15] D. Reitze *et al.*, Cosmic Explorer: The U.S. contribution to gravitational-wave astronomy beyond LIGO, Bull. Am. Astron. Soc. **51**, 035 (2019).

[16] G. Hobbs *et al.*, The international pulsar timing array project: Using pulsars as a gravitational wave detector, Classical Quantum Gravity **27**, 084013 (2010).

[17] G. Janssen *et al.*, Gravitational wave astronomy with the SKA, Proc. Sci. AASKA14 (**2015**) 037.

[18] Z. Arzoumanian *et al.* (NANOGrav Collaboration), The NANOGrav 12.5 yr data set: Search for an isotropic stochastic gravitational-wave background, Astrophys. J. Lett. **905**, L34 (2020).

[19] B. Goncharov *et al.*, On the evidence for a common-spectrum process in the search for the nanohertz gravitational-wave background with the Parkes Pulsar Timing Array, Astrophys. J. Lett. **917**, L19 (2021).

[20] H. Li *et al.*, Probing primordial gravitational waves: Ali CMB Polarization Telescope, Natl. Sci. Rev. **6**, 145 (2019).

[21] J. Antoniadis *et al.*, The International Pulsar Timing Array second data release: Search for an isotropic gravitational wave background, Mon. Not. R. Astron. Soc. **510**, 4873 (2022).

[22] P. Ade *et al.* (BICEP2 and Keck Array Collaborations), Improved constraints on cosmology and foregrounds from BICEP2 and Keck array cosmic microwave background data with inclusion of 95 GHz band, Phys. Rev. Lett. **116**, 031302 (2016).

[23] H. Hui *et al.*, BICEP array: A multi-frequency degree-scale CMB polarimeter, Proc. SPIE Int. Soc. Opt. Eng. **10708**, 1070807 (2018).

[24] K. Abazajian *et al.*, CMB-S4 science case, reference design, and project plan, arXiv:1907.04473.

[25] Y. B. Zeldovich, I. Y. Kobzarev, and L. B. Okun, Cosmological consequences of the spontaneous breakdown of discrete symmetry, Zh. Eksp. Teor. Fiz. **67**, 3 (1974).

[26] A. Vilenkin, Gravitational field of vacuum domain walls and strings, Phys. Rev. D **23**, 852 (1981).

[27] G. B. Gelmini, M. Gleiser, and E. W. Kolb, Cosmology of biased discrete symmetry breaking, Phys. Rev. D **39**, 1558 (1989).

[28] D. Coulson, Z. Lalak, and B. A. Ovrut, Biased domain walls, Phys. Rev. D **53**, 4237 (1996).

[29] T. Hiramatsu, M. Kawasaki, K. Saikawa, and T. Sekiguchi, Axion cosmology with long-lived domain walls, J. Cosmol. Astropart. Phys. 01 (2013) 001.

[30] T. Hiramatsu, M. Kawasaki, and K. Saikawa, On the estimation of gravitational wave spectrum from cosmic domain walls, J. Cosmol. Astropart. Phys. 02 (2014) 031.

[31] J. Garcia-Bellido, D. G. Figueroa, and A. Sastre, A gravitational wave background from reheating after hybrid inflation, Phys. Rev. D **77**, 043517 (2008).

[32] T. Krajewski, J. H. Kwapisz, Z. Lalak, and M. Lewicki, Stability of domain walls in models with asymmetric potentials, Phys. Rev. D **104**, 123522 (2021).

[33] K. Saikawa, A review of gravitational waves from cosmic domain walls, Universe **3**, 40 (2017).

[34] M. Dine, F. Takahashi, and T. T. Yanagida, Discrete R symmetries and domain walls, J. High Energy Phys. 07 (2010) 003.

[35] N. Chen, T. Li, and Y. Wu, The gravitational waves from the collapsing domain walls in the complex singlet model, J. High Energy Phys. 08 (**2020**) 117.

[36] N. Chen, T. Li, Z. Teng, and Y. Wu, Collapsing domain walls in the two-Higgs-doublet model and deep insights from the EDM, J. High Energy Phys. 10 (2020) 081.

[37] R. Zhou, J. Yang, and L. Bian, Gravitational waves from first-order phase transition and domain wall, J. High Energy Phys. 04 (2020) 071.

[38] S. Blasi and A. Mariotti, Domain walls seeding the electroweak phase transition, Phys. Rev. Lett. **129**, 261303 (2022).

[39] B. Barman, D. Borah, A. Dasgupta, and A. Ghoshal, Probing high scale Dirac leptogenesis via gravitational waves from domain walls, Phys. Rev. D **106**, 015007 (2022).

[40] G. B. Gelmini, S. Pascoli, E. Vitagliano, and Y.-L. Zhou, Gravitational wave signatures from discrete flavor symmetries, J. Cosmol. Astropart. Phys. 02 (2021) 032.

[41] G. B. Gelmini, A. Simpson, and E. Vitagliano, Gravitational waves from axionlike particle cosmic string-wall networks, Phys. Rev. D **104**, 061301 (2021).

[42] Y. Wu, K.-P. Xie, and Y.-L. Zhou, Classification of Abelian domain walls, Phys. Rev. D **106**, 075019 (2022).
[43] H. Jiang, T. Liu, S. Sun, and Y. Wang, Echoes of inflationary first-order phase transitions in the CMB, Phys. Lett. B **765**, 339 (2017).
[44] H. An, K.-F. Lyu, L.-T. Wang, and S. Zhou, A unique gravitational wave signal from phase transition during inflation*, Chin. Phys. C **46**, 101001 (2022).
[45] H. An, K.-F. Lyu, L.-T. Wang, and S. Zhou, Gravitational waves from an inflation triggered first-order phase transition, J. High Energy Phys. 06 (2022) 050.
[46] T. W. B. Kibble, Topology of cosmic domains and strings, J. Phys. A **9**, 1387 (1976).
[47] W. H. Zurek, Cosmological experiments in superfluid helium?, Nature (London) **317**, 505 (1985).
[48] H. Murayama and J. Shu, Topological dark matter, Phys. Lett. B **686**, 162 (2010).
[49] D. Baumann, Inflation, in *Theoretical Advanced Study Institute in Elementary Particle Physics: Physics of the Large and the Small* (World Scientific Publishing, Singapore, 2011), pp. 523–686.
[50] J. Garcia-Bellido, M. Garcia Perez, and A. Gonzalez-Arroyo, Symmetry breaking and false vacuum decay after hybrid inflation, Phys. Rev. D **67**, 103501 (2003).
[51] D. Polarski and A. A. Starobinsky, Semiclassicality and decoherence of cosmological perturbations, Classical Quantum Gravity **13**, 377 (1996).
[52] J. Lesgourgues, D. Polarski, and A. A. Starobinsky, Quantum to classical transition of cosmological perturbations for nonvacuum initial states, Nucl. Phys. **B497**, 479 (1997).
[53] C. Kiefer, D. Polarski, and A. A. Starobinsky, Quantum to classical transition for fluctuations in the early universe, Int. J. Mod. Phys. D **07**, 455 (1998).
[54] R.-G. Cai, S. Pi, and M. Sasaki, Universal infrared scaling of gravitational wave background spectra, Phys. Rev. D **102**, 083528 (2020).
[55] J. T. Giblin and E. Thrane, Estimates of maximum energy density of cosmological gravitational-wave backgrounds, Phys. Rev. D **90**, 107502 (2014).
[56] B. Spokoiny, Deflationary universe scenario, Phys. Lett. B **315**, 40 (1993).
[57] P. J. E. Peebles and A. Vilenkin, Quintessential inflation, Phys. Rev. D **59**, 063505 (1999).
[58] R. T. Co, D. Dunsky, N. Fernandez, A. Ghalsasi, L. J. Hall, K. Harigaya, and J. Shelton, Gravitational wave and CMB probes of axion kination, J. High Energy Phys. 09 (2022) 116.
[59] Y. Gouttenoire, G. Servant, and P. Simakachorn, Kination cosmology from scalar fields and gravitational-wave signatures, arXiv:2111.01150.
[60] A. Berera and L.-Z. Fang, Thermally induced density perturbations in the inflation era, Phys. Rev. Lett. **74**, 1912 (1995).
[61] A. Berera, Warm inflation, Phys. Rev. Lett. **75**, 3218 (1995).
[62] E. Forest and R. D. Ruth, Fourth-order symplectic integration, Physica (Amsterdam) **43D**, 105 (1990).
[63] H. Yoshida, Construction of higher order symplectic integrators, Phys. Lett. A **150**, 262 (1990).
[64] Z. Huang, The art of lattice and gravity waves from preheating, Phys. Rev. D **83**, 123509 (2011).
[65] D. G. Figueroa, J. Garcia-Bellido, and A. Rajantie, On the transverse-traceless projection in lattice simulations of gravitational wave production, J. Cosmol. Astropart. Phys. 11 (2011) 015.